12-2022

Global Sporadic-E Occurrence Rate Climatology Using GPS Radio Occultation and Ionosonde Data

Travis J. Hodos

Omar A. Nava

Eugene V. Dao

Daniel J. Emmons
Air Force Institute of Technology

Recommended Citation

Hodos, T. J., Nava, O. A., Dao, E. V., & Emmons, D. J. (2022). Global sporadic-e occurrence rate climatology using gps radio occultation and ionosonde data. Journal of Geophysical Research: Space Physics, 127(12). https://doi.org/10.1029/2022JA030795

JGR Space Physics

RESEARCH ARTICLE
10.1029/2022JA030795

Global Sporadic-E Occurrence Rate Climatology Using GPS Radio Occultation and Ionosonde Data

Travis J. Hodos[1], Omar A. Nava[1], Eugene V. Dao[2], and Daniel J. Emmons[1]

[1]Department of Engineering Physics, Air Force Institute of Technology, Wright-Patterson AFB, OH, USA, [2]Space Vehicles Directorate, Air Force Research Laboratory, Albuquerque, NM, USA

Key Points:

- An updated global sporadic-E climatology is presented for two intensity thresholds using a combination of global positioning satellite radio occultation and ionosonde observations
- Peak rates of 50% for blanketing E_s with no intensity threshold and 25% for moderate-E_s are observed in mid-latitudes during local summer
- Global trends are similar for both thresholds with high-latitude sporadic-E shown to be stronger but less frequent

Correspondence to:
D. J. Emmons,
daniel.emmons@afit.edu

Citation:
Hodos, T. J., Nava, O. A., Dao, E. V., & Emmons, D. J. (2022). Global sporadic-E occurrence rate climatology using GPS radio occultation and ionosonde data. *Journal of Geophysical Research: Space Physics*, *127*, e2022JA030795. https://doi.org/10.1029/2022JA030795

Received 1 JUL 2022
Accepted 7 DEC 2022

Author Contributions:
Conceptualization: Travis J. Hodos, Omar A. Nava, Eugene V. Dao, Daniel J. Emmons
Formal analysis: Travis J. Hodos, Daniel J. Emmons
Funding acquisition: Daniel J. Emmons
Investigation: Travis J. Hodos, Omar A. Nava, Eugene V. Dao, Daniel J. Emmons
Methodology: Travis J. Hodos, Omar A. Nava, Eugene V. Dao
Software: Travis J. Hodos
Supervision: Daniel J. Emmons
Writing – original draft: Travis J. Hodos
Writing – review & editing: Omar A. Nava, Eugene V. Dao, Daniel J. Emmons

Abstract An updated global climatology of blanketing sporadic E (E_s) is developed from a combined data set of Global Positioning System (GPS) radio occultation (RO) and ground-based ionosonde soundings over the period of September 2006–January 2019. A total of 46 sites and 3.2 million total soundings from the Global Ionosphere Radio Observatory network in combination with 3.0 million occultations from the Constellation Observing System for Meteorology, Ionosphere, and Climate constellation are used to calculate global occurrence rates (ORs) for two blanketing frequency thresholds: all blanketing sporadic-E with no limit on intensity (all-E_s) and moderate-E_s with fbEs $\geq$ 3 MHz. Following the GPS-RO to ionosonde comparison by Carmona et al. (2022), https://doi.org/10.3390/rs14030581 the all-E_s rates are calculated using ionosonde data and an amplitude-based S_4 threshold for the GPS-RO data while the moderate-E_s rates use a primarily phase-based technique. Occurrence rates are separated by intensity, season, month, and solar local time for quiet geomagnetic conditions. Overall, the general geomagnetic trends agree with previous E_s climatologies and the ORs peak near 50% for all-E_s and 25% for moderate-E_s measured in the mid-latitudes during local summer in the late afternoon. Low ORs are observed near the South Atlantic Anomaly and North America, and a general asymmetry is observed between hemispheres with higher ORs in the Northern Hemisphere. High-latitude and late morning blanketing E_s are found to be stronger but less frequent with rates nearly equal to the moderate-E_s mid-latitude maximums.

Plain Language Summary A global climatology for sporadic-E occurrence is developed using a combination of GPS radio occultation and ionosonde measurements for two intensity thresholds. The global OR trends generally follow the results of many previous studies with peaks in the mid-latitudes of the local summer hemisphere during late afternoon. However, the OR magnitudes differ from previous studies as the inclusion of ionosonde data provides a "ground-truth" to determine the best Global positioning satellite radio occultation technique for a given intensity threshold. From this, peak occurrence rates of nearly 50% are observed for sporadic-E with no lower limit on intensity, and 25% for moderate intensity blanketing sporadic-E.

1. Introduction

The ionosphere is a complex domain for electromagnetic dependent operations, such as global navigation satellite systems (GNSS) and High Frequency (HF) communications. Sporadic-E (E_s) layers within the E-region of the ionosphere can present a significant perturbation from the background ion content (Haldoupis, 2011; Schunk & Nagy, 2009). E_s can cause signal degradation or complete black outs for HF, Ultra High Frequency (UHF), and Very High Frequency (VHF) bands (Davies & Hartmann, 1997; Rice et al., 2011; Zeng & Sokolovskiy, 2010). Several GNSS and HF applications (such as over-the-horizon radar, polar HF communications, low earth orbit (LEO) satellite navigation, etc.) are significantly impacted by the presence of E_s, sometimes rendering the technology unusable (Buchert et al., 2015; Coleman, 1998; Headrick et al., 2008; Kintner et al., 2007; Neubeck, 1996; Rice et al., 2011; Ritchie & Honary, 2009; Zeng & Sokolovskiy, 2010).

E_s is characterized by an unusually strong concentration of metallic ions in the E-layer of the ionosphere (Schunk & Nagy, 2009; Whitehead, 1989). Spatially, E_s typically form as non-uniform, cloud like turbulent structures between 90 and 120 km in altitude (Cathey, 1969; Hysell et al., 2009; Maeda & Heki, 2015; Zeng & Sokolovskiy, 2010). Two primary conditions are typically required to form moderate-E_s layers: metal deposits from meteoric ablation and vertical convergence through neutral wind shear. E_s chemistry is driven by meteoric ablation, which deposits iron (Fe), magnesium (Mg), and other metallic ions (Ceplecha et al., 1998), and recombination rates for Mg^+ and Fe^+ are much slower than the background ions due to rapid charge exchange rates with

O_2^+ and NO^+ (Bates & Dalgarno, 1962; MacDougall et al., 2000). Diurnal and semidiurnal tides provide wind shears that vertically compress the long-lived metallic ions through the Lorentz force (Haldoupis, 2011).

Measuring E_s formation globally is a challenging task. Perhaps the most detailed observations of the ionosphere are through incoherent scatter radars (ISRs; Mathews, 1998). While ISRs provide excellent spatial detail, there are few sites around the globe nullifying their ability to create a global E_s climatology. Ionosondes also provide direct E_s observations with a somewhat loose global coverage (Matsushita & Reddy, 1967; Reinisch & Galkin, 2011; Whitehead, 1972). Previous E_s climatologies have been completed using only ionosondes (Merriman et al., 2021; Smith, 1957), but global interpolation is difficult with land-locked and irregularly spread ionosondes.

Global Positioning System radio occultation (GPS-RO) is a viable alternative to both ISR and ionosondes to provide dense global coverage of E_s. GPS-RO is a technique in which the transmitted GPS L1 (1.575 GHz) and L2 (1.227 GHz) signals are measured by a LEO satellite, and atmospheric characteristics are derived using the signals' amplitude and phase perturbations. The first Constellation Observing Satellite for Meteorology, Ionosphere, and Climate (COSMIC-1) provided an average of nearly 2,000 global occultations per day over the 13 year period from 2006 to 2019 (Rocken et al., 2000; Schreiner et al., 2014) from six LEO satellites in circular orbits with inclinations of 72° and altitudes of 800 km (Fong et al., 2008).

While GPS-RO provides a solution to the global coverage problem inherent in the ISR and ionosonde data sets, the detection of E_s is not straightforward and occurrence rates (ORs) from many previous studies vary widely (Gooch et al., 2020; Luo et al., 2021; Tsai et al., 2018; Wu et al., 2005; Yeh et al., 2014; Yu et al., 2019, 2020). For example, comparing results from Chu et al. (2014) and Arras and Wickert (2018), maximum E_s ORs for similar periods differ by approximately 40%. This large difference in OR magnitudes is likely due to distinct E_s intensity thresholds for the two techniques.

To investigate the OR differences between studies and remove ambiguities, Carmona et al. (2022) compared five GPS-RO techniques (Arras & Wickert, 2018; Chu et al., 2014; Gooch et al., 2020; Niu et al., 2019; Yu et al., 2020) against ionosonde measurements as the ground-truth, in the form of Digisonde observations from Merriman et al. (2021). This comparison found the Chu et al. (2014) phase perturbation technique to most accurately predict E_s with fbEs $\geq$ 3 MHz (moderate-E_s), and the Yu et al. (2020) S_4 amplitude perturbation technique to most accurately predict any occurrence of E_s with no lower limit on intensity (all-E_s). While the Chu et al. (2014) technique also includes a small amplitude perturbation, the limiting factor for E_s measurement is in the phase requirements.

Here, we combine the results of Merriman et al. (2021) and Carmona et al. (2022) to develop a global climatology of E_s occurrence for two fbEs intensity thresholds using both GPS-RO and ionosonde data. Occurrence rates are separated by intensity threshold to provide insight into probabilities of disruption for ionospheric radio wave propagation, as the dispersive nature of the plasma delivers a larger impact for elevated plasma frequencies. Separating by E_s intensity allows probabilistic disruption estimates for varying levels of severity, which is particularly helpful to HF communication and radar operations. Section 2 describes the data set and all background information relevant to developing the climatology. Section 3 presents the global climatology for annual, seasonal, monthly, and diurnal sporadic-E occurrence. Section 4 discusses the differences between the two E_s detection methods, and the implications in the high-latitudes. A subsequent paper will explore the implications of varying geomagnetic and solar conditions on the development of E_s.

2. Ionosonde and GPS-RO Data

Chu et al. (2014) introduced a primarily phase-based binary check for E_s using COSMIC 1 Hz ionospheric phase (ionPhs) data available through the COSMIC Data Analysis and Archive Center (CDAAC; https://cdaac-www.cosmic.ucar.edu/). After applying a high pass filter, the detrended L1 and L2 GPS signals are required to meet the following three criteria to predict the existence of E_s:

1. The magnitude of the L1 and L2 phase perturbations must be $\geq$5 cm.
2. The ratio of L1 excess phase (ΔL1) to L2 excess phase (ΔL2) must be between 1.5 and 1.8.
3. The L1 amplitude perturbation must be >0.01.

Carmona et al. (2022) used a slightly looser $\Delta L1/\Delta L2$ of 1.2–1.9 and this study uses the same range. The phase perturbation in the first step is an initial check to make sure the E_s layer met a minimum length/intensity threshold.

Since the excess phase is related to the inverse square of the carrier frequency, the ratio of ΔL1/ΔL2 would ideally equal 1.65, so the 1.2–1.9 buffer allows for slight variation due to differences in ray paths and/or diffractive effects. The third step checks for an amplitude deviation from the background noise to ensure a clearly defined E_s layer. It must be noted that this amplitude deviation is satisfied for many occultations without sporadic-E and the limiting factor is the phase ratio in Step 2 likely due to differences in ray paths for L1 and L2 (Carmona et al., 2022). From 2006 to 2019, there are 1.3 million ionPhs observations used to calculate moderate-E_s ORs.

Yu et al. (2020) compared foEs measurements from 25 ground-based ionosondes with $S_{4,\,max}$ calculated from COSMIC GPS-RO during the period 2006–2014. The technique uses 1 Hz S_4 from L1 amplitude measurements and extracts the maximum value, $S_{4,\,max}$, which can be converted to an foEs through the following empirical relationship:

$$(\mathrm{foEs}[MHz] - 1.2)^2 = 13.62 \times S_{4,\max}\,. \tag{1}$$

Carmona et al. (2022) used the same formula to calculate fbEs by applying a binary foEs cutoff of (foEs − 1.2) = 3 MHz. GPS-RO techniques for monitoring sporadic-E depend on the metallic ion perturbation to the background ionosphere, such that this criterion is essentially foμEs = 3 MHz as outlined by Haldoupis (2019). It must be noted that while fbEs and foEs have different physical meanings with respect to ionosonde measurements (Reddy & Mukunda Rao, 1968), we use Equation 1 as a proxy for fbEs while noting that fbEs ≤ foEs. Therefore, the binary cutoff in terms of an fbEs can be recast as (fbEs − 1.2) ≤ 3 MHz. While this cutoff was originally selected to compare against the moderate-E_s data set, it was found to agree best with the fbEs ORs without an intensity threshold. Additionally, it must be noted that the $S_{4,\,max}$ calculated here and in Carmona et al. (2022) is calculated directly from the 50 Hz atmospheric phase (atmPhs) data, which is likely different from the S_4 provided directly from CDAAC (see Syndergaard, 2006). From 2006 to 2019, there are 1.7 million atmPhs observations used to calculate all-E_s ORs from the Yu et al. (2020) technique with our pre-defined threshold.

A quality control inspection is also performed on the GPS-RO data following the procedure outlined by Yang et al. (2009). This procedure places an upper limit of 1.5 on the mean deviation of the electron density profile, and here we use total electron content in place of electron density. Additionally, occultations with fewer than 400 data points for the 50 Hz data or 8 data points for the 1 Hz data are excluded from the climatology. The RO data is also limited to an altitude range where most E_s is expected to occur: 70–130 km (Chu et al., 2014; Zeng & Sokolovskiy, 2010). We do not separate E_s occurrence as a function of altitude, so the ORs provided here count all layers measured within this altitude range.

Figure 1 shows the observation density binned in 5° latitude × 5° longitude intervals, with 50 Hz atmPhs observations for all-E_s occurrence on top, and 1 Hz ionPhs observations for moderate-E_s (fbEs ≥ 3 MHz) occurrence on the bottom. At finer grid resolution (e.g., 1° × 1° or 2° × 2°), the data set is too sparse to provide compelling conclusions. Both observation density plots share the same patterns: the highest concentration of observations are between 15° and 60° latitude, and there are considerably less in the equatorial and polar regions. Due to the COSMIC orbit inclination of 72°, the orbit path traverses a smaller fraction of the equatorial region. In the polar regions the convergence of latitude lines results in smaller land areas per 5° × 5° bin. Figure 2 shows the E_s observation density, with each positive occurrence of E_s recorded as one observation. The all-E_s set is on top, the bottom is moderate-E_s, and the overlay lines are the geomagnetic latitude. While the E_s observation density is not particularly useful by itself, it helps to show the number of measurements used to calculated the ORs; over all seasons and times, the maximum number of GPS-RO derived E_s observations for one 5° × 5° bin is approximately 290 for all-E_s and 150 for moderate-E_s.

For reference, the Digisondes' total observation density is shown in Figure 3. Digisonde data was collected from the Global Ionosphere Radio Observatory web portal (http://giro.uml.edu/didbase/scaled.php) consisting of ionograms automatically scaled using the Automatic Real-Time Ionogram Scaler with True height (ARTIST; Galkin and Reinisch, 2008). Following the results of Merriman et al. (2021), only ionograms automatically scaled with ARTIST-5 were used for this global climatology. To ensure proper sampling over all local times, each ionosonde was required to be in operation for 90% of a given day to include the measurements in the analysis. In some places, like Europe, there are many Digisonde sites and some within the same 5° × 5° grid boxes. However, outside of places like Europe, the spatial limitations inherent in ionosonde measurements is quite apparent (Figure 3). Ionosondes are generally landlocked and require power, maintenance, and a dedicated facility. For this reason, there are large regions (oceans, Africa, Central Asia, etc.) without regular ionosonde soundings. Therefore, a global

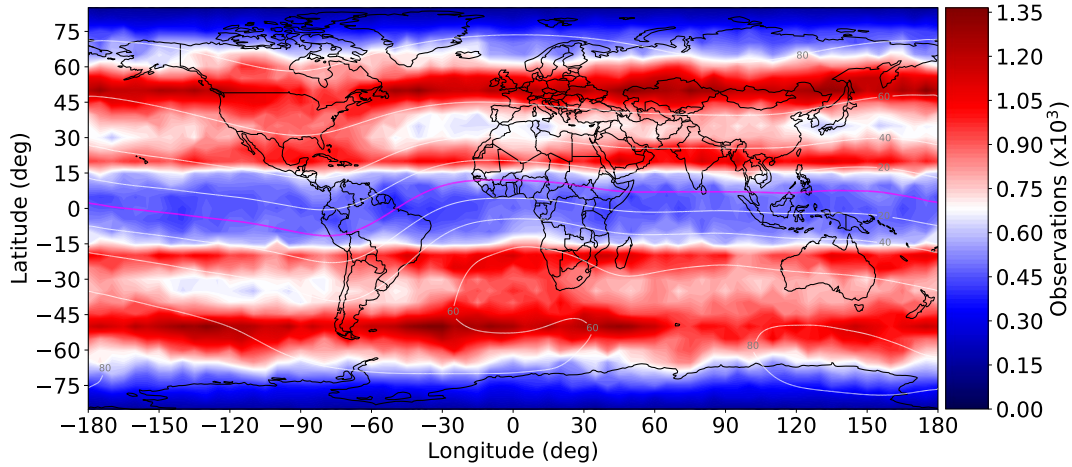

(a) All-E_s (atmPhs)

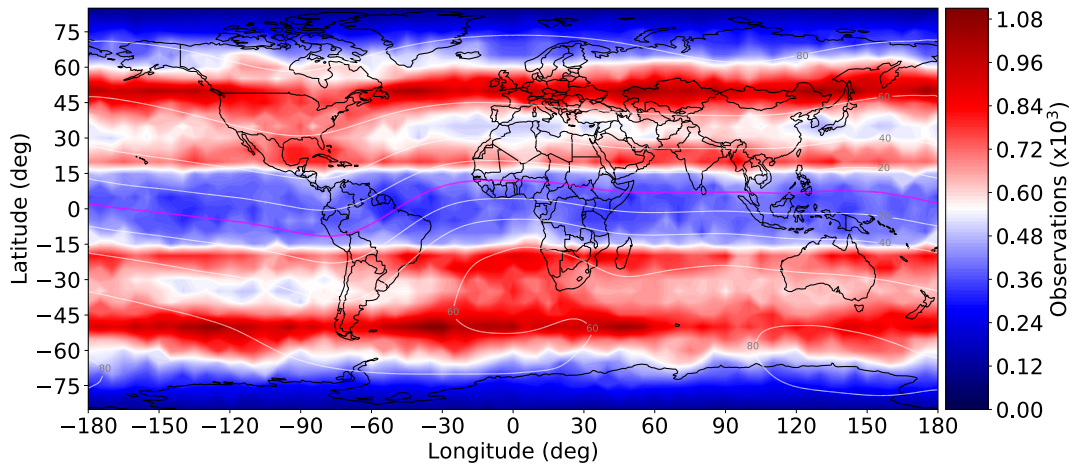

(b) Moderate-E_s (ionPhs)

Figure 1. Global positioning satellite radio occultation observation density in 5° latitude × 5° longitude bins from 2006 to 2019 for (a) 50 Hz atmPhs data set used for all-E_s (fbEs with no lower limit on magnitude) and (b) 1 Hz ionPhs data set used for moderate-E_s (fbEs ≥ 3 MHz). There is natural banding in the density due to the nature of the Constellation Observing System for Meteorology, Ionosphere, and Climate constellation orbit geometry.

climatology using only Digisonde observations relies on interpolation to cover the large gaps (Smith, 1957). Combining ionosonde and GPS-RO provides an opportunity to cover the large spatial gaps while maintaining the valuable ionosonde data as ground-truth.

For this study, ORs in each 5° × 5° bin are calculated by

$$OR_i(all|moderate) = \frac{N_{i,Digi}(all|moderate) + N_{i,RO}(all|moderate)}{N_{i,Digi} + N_{i,RO}}, \quad (2)$$

where OR_i (all|moderate) is the OR for the *i*'th latitude/longitude bin and intensity threshold, $N_{i,\mathrm{Digi}}$ (all|moderate) and $N_{i,\mathrm{RO}}$ (all|moderate) are the number of positive Digisonde and GPS-RO E_s measurements during the period of interest above the desired intensity threshold, and $N_{i,\mathrm{Digi}}$ and $N_{i,\mathrm{RO}}$ are the total number of Digisonde and GPS-RO measurements in the bin during the period of interest. Here, $N_{i,\mathrm{RO}}$ (all) represents the number of occultations that trigger the Yu et al. (2020) technique while $N_{i,\mathrm{RO}}$ (moderate) is the number that satisfy the Chu et al. (2014) criteria. For ionosonde measurements, we use fbEs ≥ 3 MHz to satisfy $N_{i,\mathrm{Digi}}$ (moderate) and any blanketing E_s measurement for $N_{i,\mathrm{Digi}}$ (all). Also, we provide each measurement with equal weighting as an arbitrary weighting

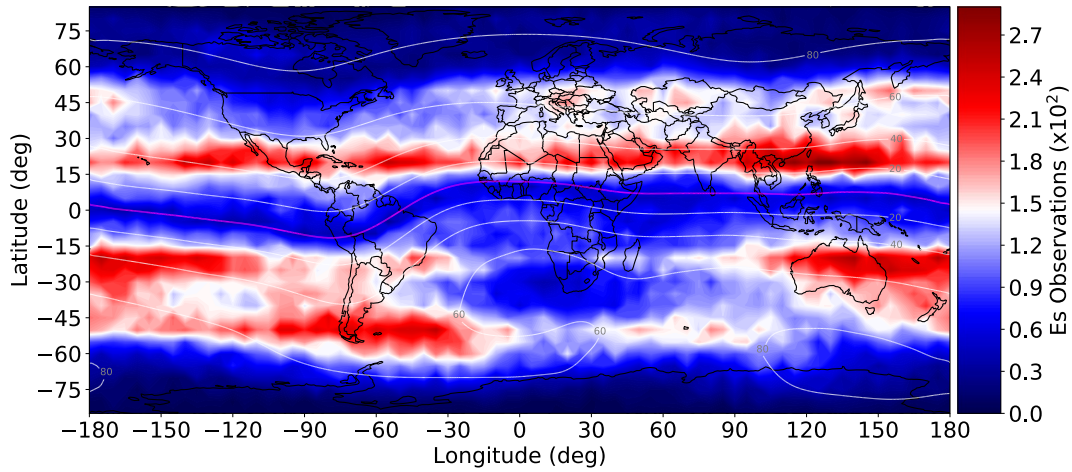

(a) All-E_s (atmPhs)

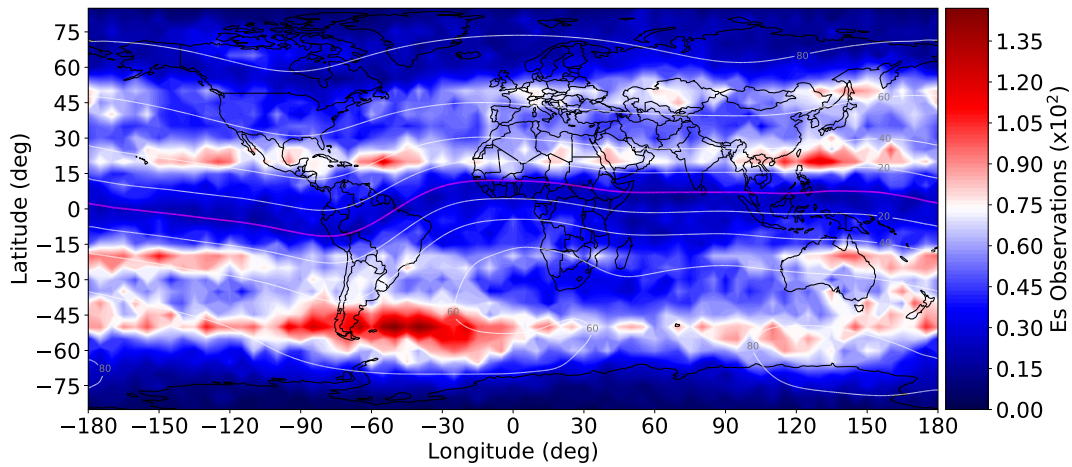

(b) Moderate-E_s (ionPhs)

Figure 2. Global positioning satellite radio occultation E_s observation density for (a) all-E_s and (b) moderate-E_s. Similar to the standard observation density map (Figure 1), the mid-latitudes offer the highest density of E_s observations.

between ionosonde and GPS-RO measurements would be difficult to determine and justify. However, due the considerable number of ionosonde observations in a bin relative to the number of GPS-RO observations, bins containing ionosondes are heavily weighted toward ionosonde derived ORs. It must also be noted that temporal averaging removes fluctuations that occur over shorter time periods, which may be important for certain applications.

To establish a baseline for a global climatology, it is important that the analysis have consistent background conditions. Therefore, all results presented here include only observations taken during geomagnetic quiet conditions with respect to the Kp and AE indices. A subsequent article will explore the effects of altering geomagnetic and solar conditions on the E_s global climatology. For the Kp index, quiet was defined as Kp $\leq$ 4 following the Space Weather Prediction Center's scales for geomagnetic activity (https://www.swpc.noaa.gov/noaa-scales-explanation). Likewise, AE < 200 nT was considered quiet in agreement with Kamide and Akasofu (1983). Any observations taken during a geomagnetically active day, as recorded in the OMNIWeb database (https://omniweb.gsfc.nasa.gov/form/dx1.html), were not used.

For the entire analysis, a minimum observation threshold was used to cap the error at 10%. Since E_s ORs are calculated by dividing the number of E_s observations by total observations, each observation is a single binary

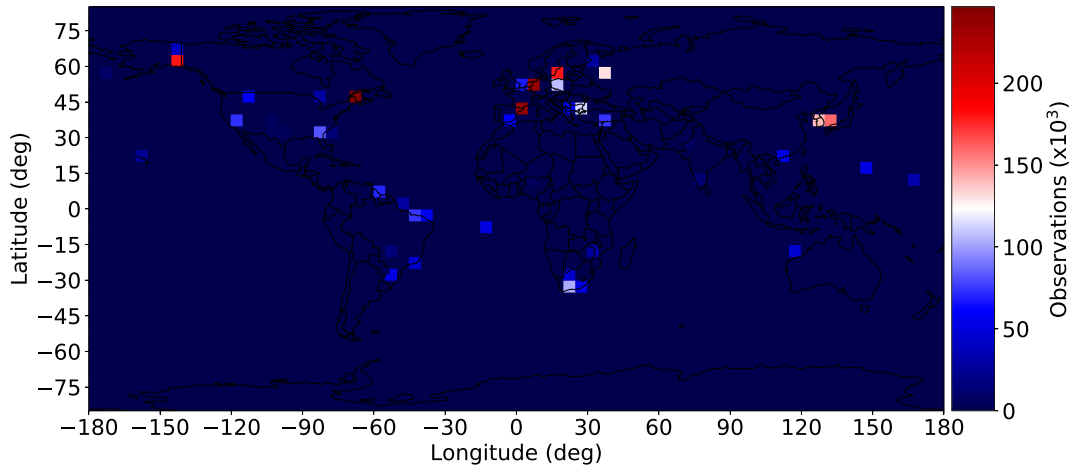

Figure 3. The global distribution of Digisonde observations within 5° longitude × 5° latitude bins. Note, some bins contain multiple Digisonde sites, as displayed by the large number of observations in bins over Europe.

event. The accumulation of single population binary events creates a Bernoulli distribution (Binary distribution with a trial size of 1) with a standard deviation, σ_i, of

$$\sigma_i = \sqrt{OR_i(1 - OR_i)}, \tag{3}$$

where OR_i is the E_s OR for the i'th latitude/longitude bin. The standard error, $\sigma_{s,i}$, for the distribution is

$$\sigma_{s,i} = \frac{\sigma_i}{\sqrt{N_i}}, \tag{4}$$

where N_i is the population size (number of observations in a particular bin). The standard error is capped at 10% by requiring $N_i \geq 25$ for all spatial and temporal bins. Error is maximized when the rate is 50%, which yields a σ_i of 0.5. Therefore, to ensure the standard error rate for the study is less than 10%, we require $N_i \geq 25$.

In addition to the standard error, sporadic-E measurement errors exist for both GPS-RO (Gooch et al., 2020) and ionosondes (Reddy & Mukunda Rao, 1968). The path-integrated nature of RO measurements provides an inherent uncertainty to the inversion results (Yue et al., 2013), and uncertainties in length, orientation, and vertical thickness can produce ambiguities in interpreting the signal perturbations caused by sporadic-E (Stambovsky et al., 2021; Zeng & Sokolovskiy, 2010). While ionosonde E_s measurements are more direct, our reliance on automatic scaling software such as ARTIST induces additional uncertainties (Bossy, 1994). Further, the lower limit of ∼1.5 MHz for ionosonde measurements due to frequency allocation and sensitivity imposes a threshold for measurable E_s intensity using vertical soundings that can be site dependent. A long-term comparison of ionosonde derived E_s ORs between manual and automatic scaling would help to quantify the ionosonde uncertainties, but we are not aware of the existence of such a comparison. However, if we use ionosonde derived ORs as the ground-truth, the uncertainties of the RO techniques employed here are explored in detail in Carmona et al. (2022).

Ionospheric phenomenon like E_s are inherently intertwined with the Earth's magnetic field through the dependence of ion convergence on the Lorentz force (Whitehead, 1989). Convergence rates depend on neutral wind shears in addition to the magnitude and orientation of the local magnetic field. For this study, the World Magnetic Model (WMM) magnetic field inclination is used as the magnetic latitude. The WMM was developed by NOAA, NGDC and CIRES and is updated every 5 years, or as needed (Maus et al., 2010). Since our data spans 2006–2019, we chose the averaged 2010 Epoch WMM main field inclination to make geomagnetic latitude contours for the maps. Inclination has some variation year to year, but the change is minor and 2010 was selected to represent the data set.

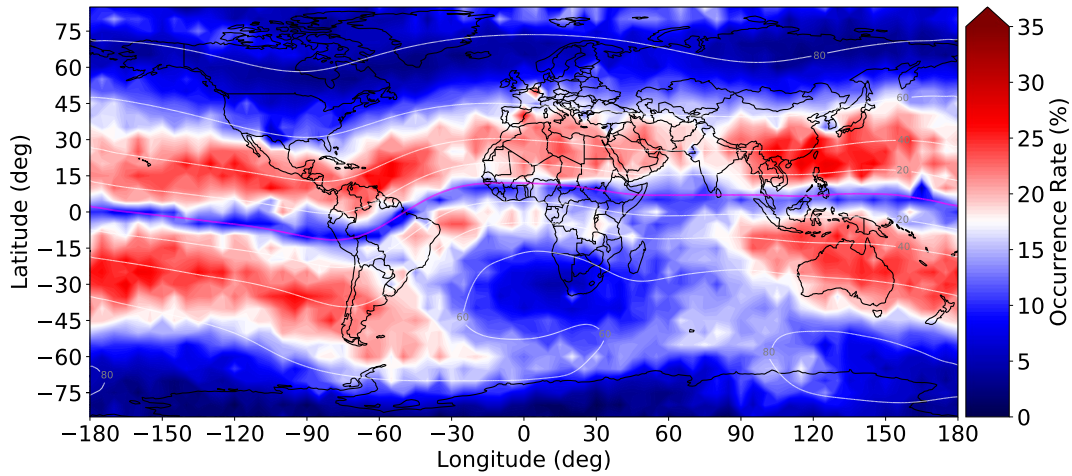

(a) All-E_s

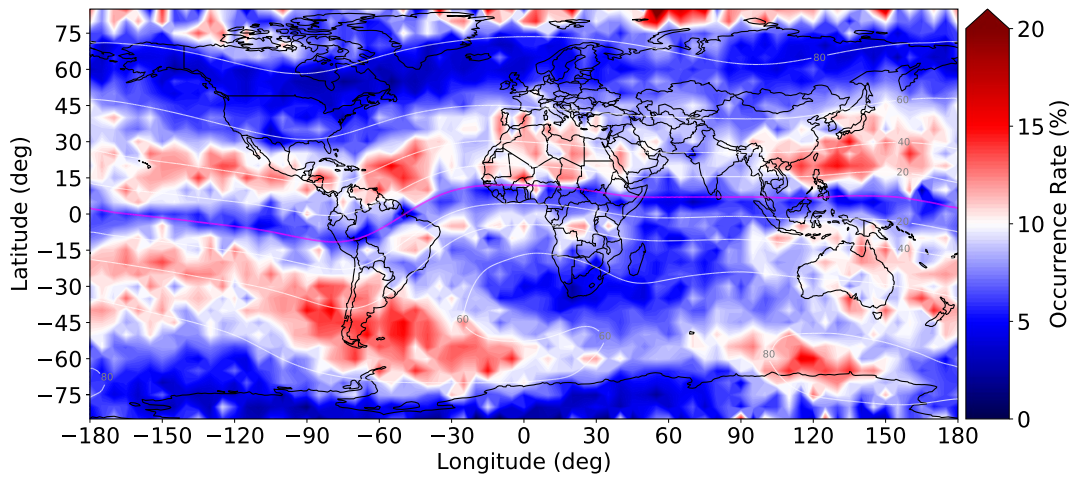

(b) Moderate-E_s

Figure 4. Annual E_s occurrence rates (ORs), with (a) All measurable blanketing E_s and (b) Moderate-E_s with fbEs ≥ 3 MHz. The E_s is mostly contained to the mid-latitudes, with low ORs along the geomagnetic equator and in between 60° and 80° inclination. In (b) the high-latitudes above 80° inclination show ORs nearly equal to the mid-latitude peaks.

3. Results

Figure 4 shows the geomagnetic quiet, annual ORs for any E_s measurable by ionosondes and GPS-RO and moderate-E_s. The ORs for all-E_s are roughly double the moderate-E_s rates, on average. The highest annual ORs are in the mid-latitudes, particularly between 10 and 60° inclination, with peak ORs of 35% for all-E_s and 20% for the 3 MHz threshold. It must be noted that the peak annual ORs are less than the seasonal or diurnal peaks because the rates are averaged over all seasons and local times, including periods with low activity. Common among both maps is the lack of blanketing E_s along the geomagnetic equator and areas greater than 60° inclination. At the geomagnetic equator and inclinations above 60°, ion convergence through wind shear is constrained as described in Haldoupis (2011). The South Atlantic Anomaly (SAA) off the southwest coast of Africa shows exceptionally low rates. By analysis of the contours, the SAA is positioned below the −60° inclination contour, which is likely the driver behind the low rates in addition to the weak geomagnetic field strengths. Also, our focus on calm geomagnetic conditions limits the influence of energetic particle induced E-region enhancements observed in the SAA (Conceição-Santos et al., 2019). In the regions greater than 80° geomagnetic latitude, the moderate-E_s rates are nearly equal to the mid-latitude maximums while the all-E_s rates are nearly half the mid-latitude peaks. This indicates that high-latitude E_s is stronger but less frequent.

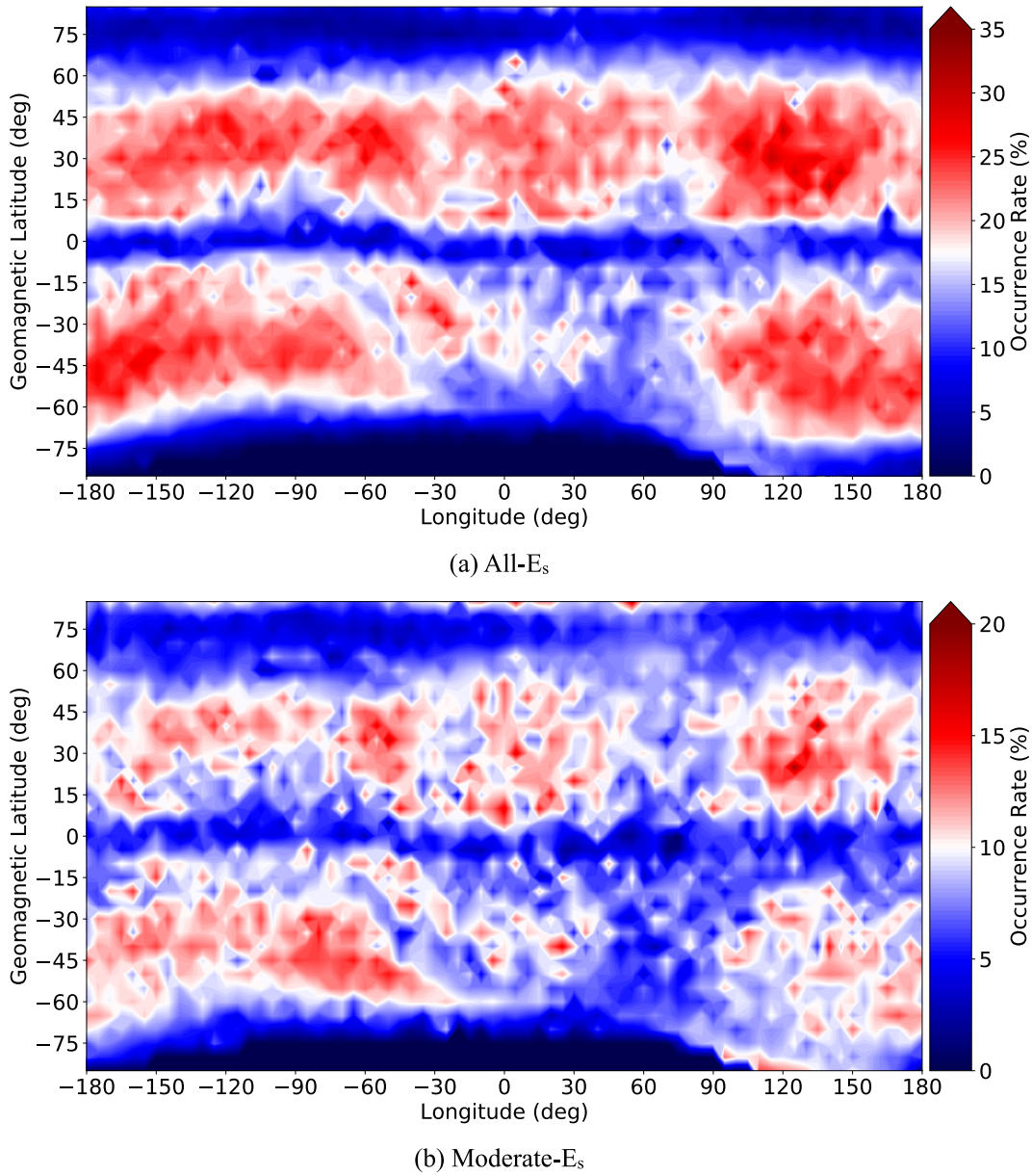

Figure 5. Annual E_s occurrence rates for geomagnetic latitude and geographic longitude for (a) All-E_s and (b) Moderate-E_s. The low E_s rate along the geomagnetic equator is obvious in this format and E_s is mostly contained between 10° and 60° geomagnetic latitude except for some high-latitude activity in the moderate-E_s map.

Figure 5 shows the global annual fbEs rates adjusted for geomagnetic latitude. Again, the all-E_s rates are roughly double the moderate-E_s rates. When adjusting for geomagnetic latitude, one can clearly see the low ORs along the equator. In addition, both techniques show elevated mid-latitude (10°–60°) rates with relatively low annual rates in the equatorial and high-latitude regions consistent with the empirical E_s model recently developed by Yu et al. (2022). The dark regions at the bottoms of Figure 5 are an artifact of using a map with geomagnetic latitude and geographic longitude. As displayed in Figure 4, the contour with geomagnetic latitude below 80° only spans a geographic longitude of approximately 100–190°, so the other geographic longitudes will not contain data for these geomagnetic latitudes.

The general trend of E_s ORs as a function of geomagnetic latitude follows the wind shear theory fairly well. In summary, diurnal and semidiurnal tidal wind shears create vertical convergence of long-lived metallic ions produced by meteoric ablation (Haldoupis, 2011; Whitehead, 1989). This process is a strong function of the

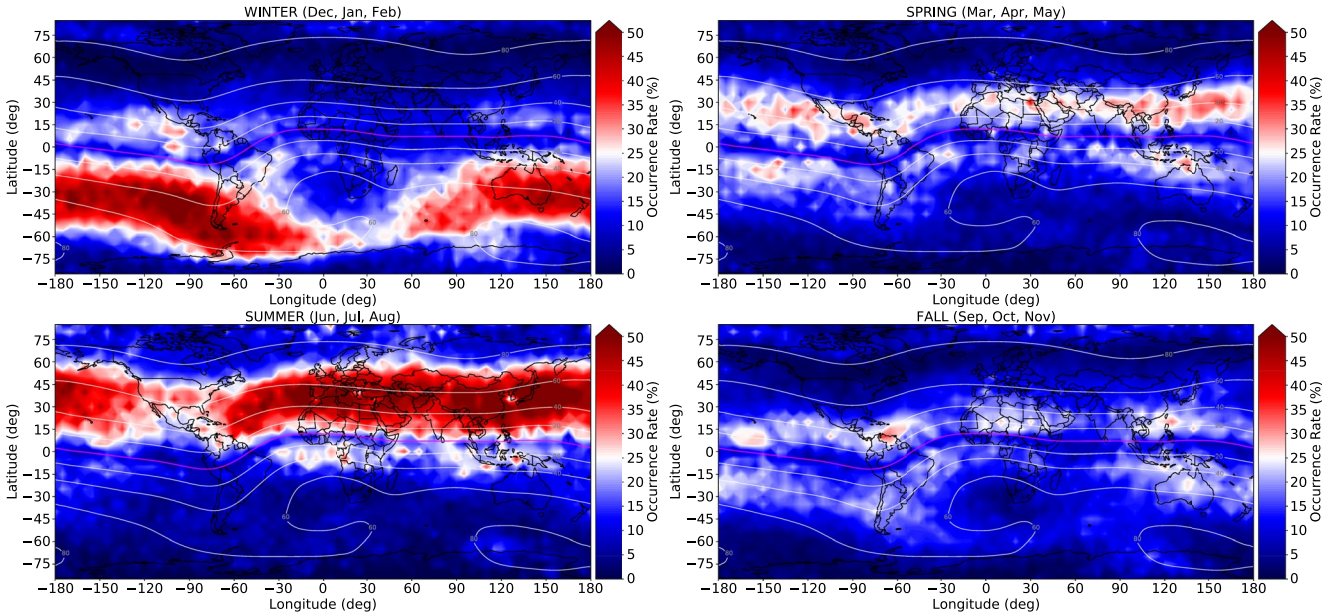

Figure 6. All-E_s occurrence rates for the four boreal seasons: winter (top left), spring (top right), summer (bottom left), and fall (bottom right).

magnetic dip angle with a maximum vertical convergence at the geomagnetic equator for zonal wind shears with no vertical convergence at the geomagnetic poles. While the wind shear convergence on metallic ions is maximized at the geomagnetic equator, the strong magnetization of electrons at E-region altitudes (Rishbeth & Garriott, 1969) constrains the electrons to horizontal motion. As the ions are transported vertically, the electrons remain at a constant altitude and a charge separation creates an electric field that limits the ions vertical motion (Chu et al., 2014). Therefore, through the wind shear theory sporadic-E formation is unlikely near the geomagnetic equator and poles, which agrees with the rates displayed in Figure 5 showing decreased activity in these regions. While E_s ORs are low near the geomagnetic equator, there is some activity from equatorial electrojet irregularities caused by the gradient instability (Whitehead, 1989). This q-type of sporadic-E is commonly measured by ionosondes near the magnetic equator (Piggott & Rawer, 1978) due to Bragg scattering of the HF signals. However, these irregularities are less likely to trigger the GPS-RO techniques employed here, which results in low but non-zero ORs over the magnetic equator.

Figure 6 shows the all-E_s seasonal ORs for each boreal season: winter (top left), spring (top right), summer (bottom left), and fall (bottom right). While the ionosonde and RO trends agree fairly well over all, there are instances where the bins dominated by ionosonde data do not perfectly align with the RO trends such as over Korea during boreal summer. This same behavior was observed in Carmona et al. (2022) which showed agreement when averaged over all sites, but also showed individual sites where the ORs did not align.

The seasonal analysis shows E_s is much more prevalent in local summer with peak ORs near 50%. To understand the seasonal dependence, we must analyze the two factors required for E_s formation: vertical wind shears and sufficient metallic ion densities. Concerning vertical wind shears, several modeling and E_s observational studies have shown a seasonal dependence with ideal conditions during local summer (Chu et al., 2014; Yu et al., 2019). Additionally, a recent study using the Michelson Interferometer for Global High-Resolution Thermospheric Imaging (MIGHTI) onboard the Ionospheric Connection Explorer (ICON) found ideal wind shears in the northern hemisphere during June–August (Yamazaki et al., 2022), experimentally verifying previously modeled results.

Concerning metallic ion densities, a theory based on local meteoric deposits peaking in the local summer (Singer et al., 2004; Younger et al., 2009) was previously used to explain the E_s seasonal variations (Haldoupis et al., 2007). However, separate meteor deposit measurements show peaks during the fall rather than summer (Janches et al., 2006) indicating that the local meteoric deposit theory does not provide a complete explanation of the seasonal variation in E_s. Recently, a study focused on lower thermospheric winds derived from RO and ionosonde measurements combined with the specified dynamics version of the Whole Atmosphere Community

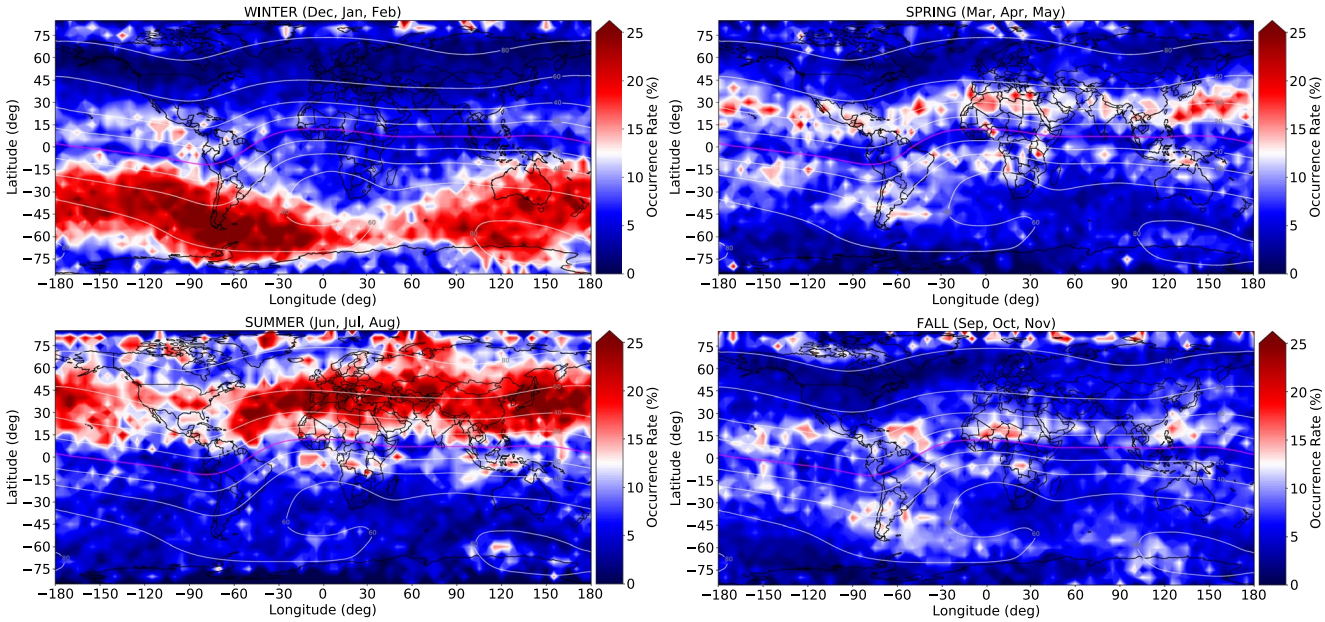

Figure 7. The moderate-E_s occurrence rates for the four boreal seasons: winter (top left), spring (top right), summer (bottom left), and fall (bottom right).

Climate Model (SD-WACCM4) found a winter-to-summer horizontal transport of metallic ions for the altitude range of ~95–115 km (Yu et al., 2021). This meridional circulation is driven by gravity-wave forcing and provides a mechanism to transport metallic ions to the summer hemisphere, thereby increasing the E_s formation rates. Through this transport mechanism, local meteor deposits can be transported globally such that the seasonal variations follow the trends in Figures 6 and 7.

During the boreal summer, there is a noticeable decrease in ORs over North America in comparison to other regions of similar latitude. This is likely due to anomalous geographical dependence of vertical wind shear shown by Shinagawa et al. (2017) using data from the atmosphere-ionosphere coupled model GAIA (Ground-to-topside model of the Atmosphere and Ionosphere for Aeronomy). Shinagawa et al. (2017) showed that GAIA developed vertical ion convergence in the summer months was on the order of 1–2 cm^{-1} less over North American than other regions of similar latitude.

Moderate-E_s ORs separated by season are displayed in Figure 7. For this moderate-E_s threshold, ORs of 25% are observed throughout a large portion of the mid-latitudes during local summer. General trends are similar for Figures 6 and 7: low ORs at the geomagnetic equator, within the SAA, and over North America, and low rates globally during the spring/fall. The high-latitude activity is more clear in the moderate-E_s maps as the rates are nearly equal to the mid-latitude maximums and only half the all-E_s mid-latitude peak rates. Of interest to note are the intense but short-lived E_s layers caused by atmospheric gravity waves discussed in Yu et al. (2019), which produce relatively large S_4 values. Additionally, Luo et al. (2021) show peak high-latitude E_s ORs derived from S_4 with magnitudes around 50% of the peak mid-latitude rates in boreal summer, which is roughly the same ratio observed here for all-E_s but over a smaller region.

Figures 8 and 9 show the global monthly blanketing E_s ORs. The same trends in the seasonal analysis are present in the monthly rates. In the Southern Hemisphere, E_s rates are largest in the austral summer months (Dec–Feb) while peak rates for the Northern Hemisphere are observed during boreal summer (Jun–Aug). Mar, Apr, Sep, and Oct are transition months where the E_s rates are globally reduced. The winter-to-summer lower thermospheric circulation patterns are readily observed in Figures 8 and 9 where the peak ORs move from the mid-latitudes through the equatorial region to the mid-latitudes in the opposite hemisphere. While the metallic ions are collected near the geomagnetic equator during fall and spring, the E_s formation in the equatorial zones is limited by the strong magnetization of electrons.

For the diurnal analysis, the ionosonde data was binned into 1-hr intervals while the temporal resolution of the RO data allows for smaller bins. To maximize the temporal resolution displayed here, we use 12 min bins for the

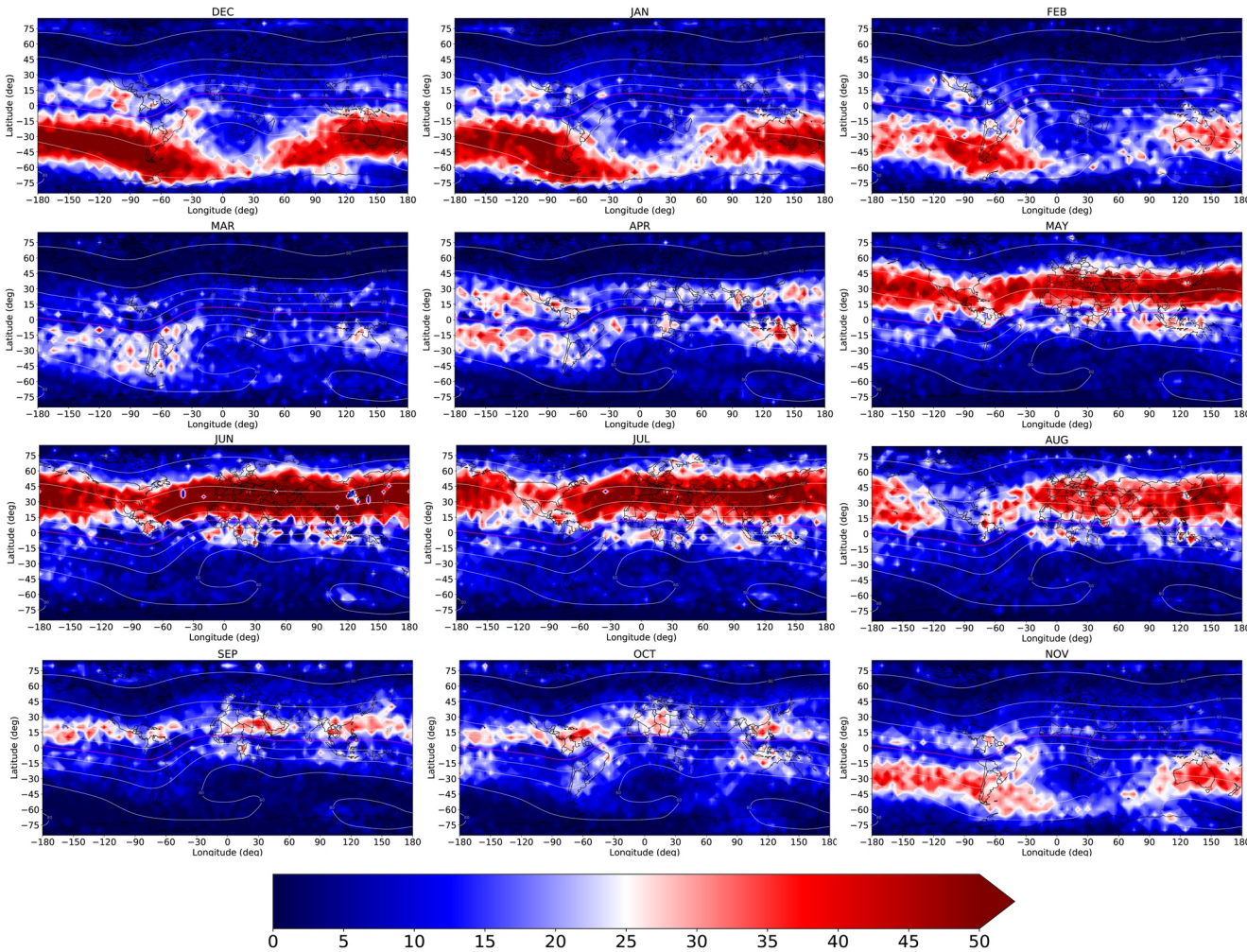

Figure 8. All-E_s occurrence rates (%) for each month, organized in rows by season.

figures. As the ionosonde data is hourly, we assume a uniform distribution over the entire hour and equally spread the number of measurements into each 12 min bin for the hour of interest. Figure 10 shows the annual diurnal variation in fbEs rates as a function of geomagnetic latitude. Geomagnetic latitudes containing ionosondes essentially show the ionosonde derived diurnal trends as the latitude bins include significantly more ionosonde than RO measurements (see Equation 2). While the diurnal trends derived from RO and ionosondes generally agree, there are latitude bands with slightly higher or lower rates where the ionosonde and RO rates do not perfectly align. This is most obvious in the moderate-E_s trends at geomagnetic latitudes such as 25° and −10° which show elevated ORs in the morning around 0900 SL that are not observed at the other latitudes. However, the diurnal and semidiurnal trends are present in both the all-E_s and moderate-E_s data sets showing mid-latitude peaks during the late morning and afternoon.

For the all-E_s data set, high ORs are observed between 1500 and 2100 SL with a peak between 1600 and 1800 SL. Peak rates occur slightly earlier for the moderate-E_s data set around 1500-1700SL for most latitudes with late morning peaks observed for several latitude bands. Early morning hours from 0100 to 0600 are characterized by low ORs for all latitudes and both intensity thresholds. The daily maximum and minimum match the 1800 SL maximum and 0600 minimum found by Yu et al. (2022) at most mid-latitudes. In the 6-hr span from 1900 to 0100 SL, the all-E_s ORs show less formation relative to the late afternoon peak than the moderate-E_s rates. This indicates that the stronger E_s layers tend to persist longer than the weaker layers.

Figures 11 and 12 show the diurnal ORs for each season. In Figure 11, blanketing E_s occurs nearly all day in the mid-latitude local summer, with a short downtime from 0200 to 0600 SL. For the remainder of the year

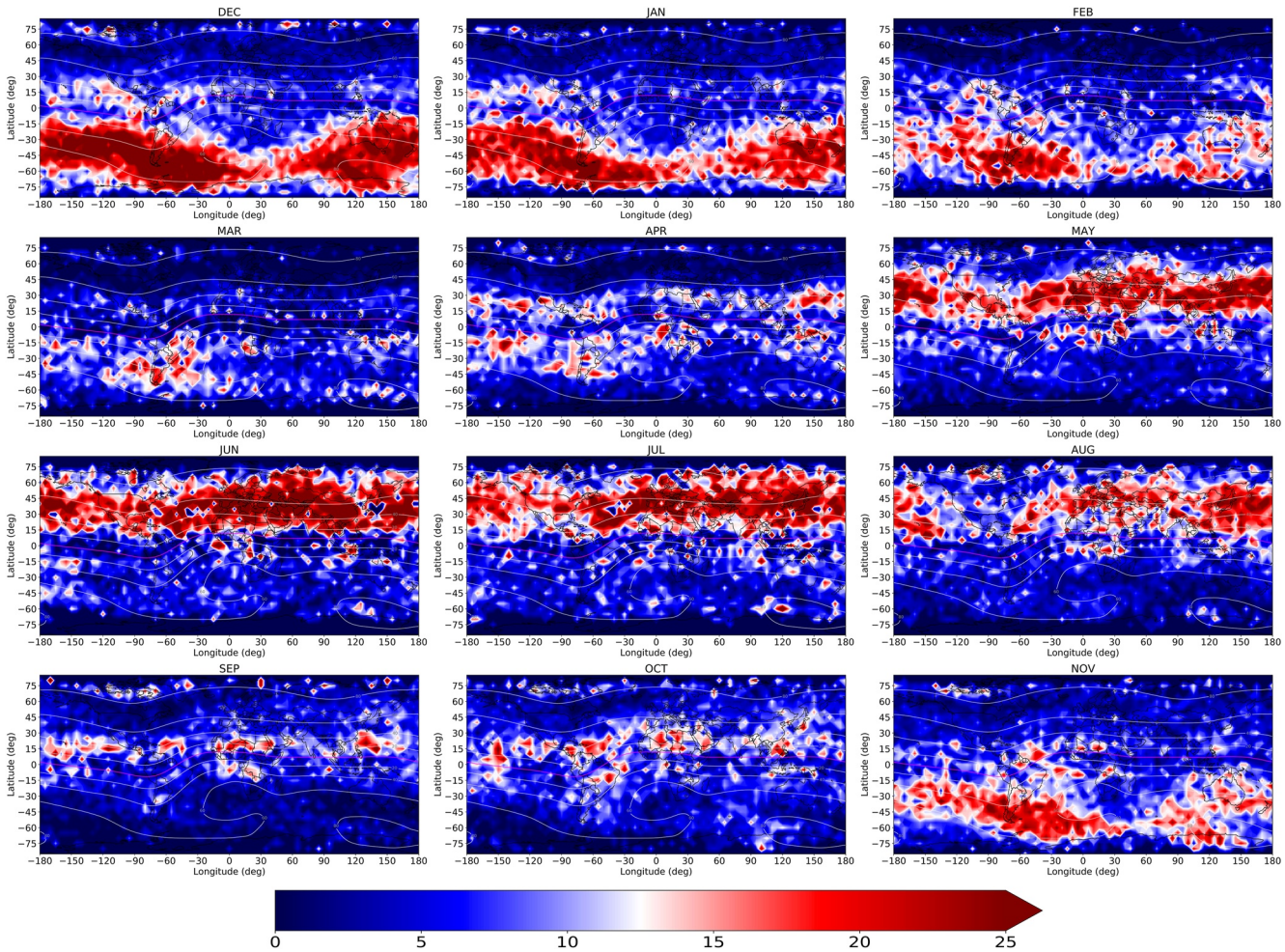

Figure 9. Moderate-E_s occurrence rates (%) for each month, organized in rows by season.

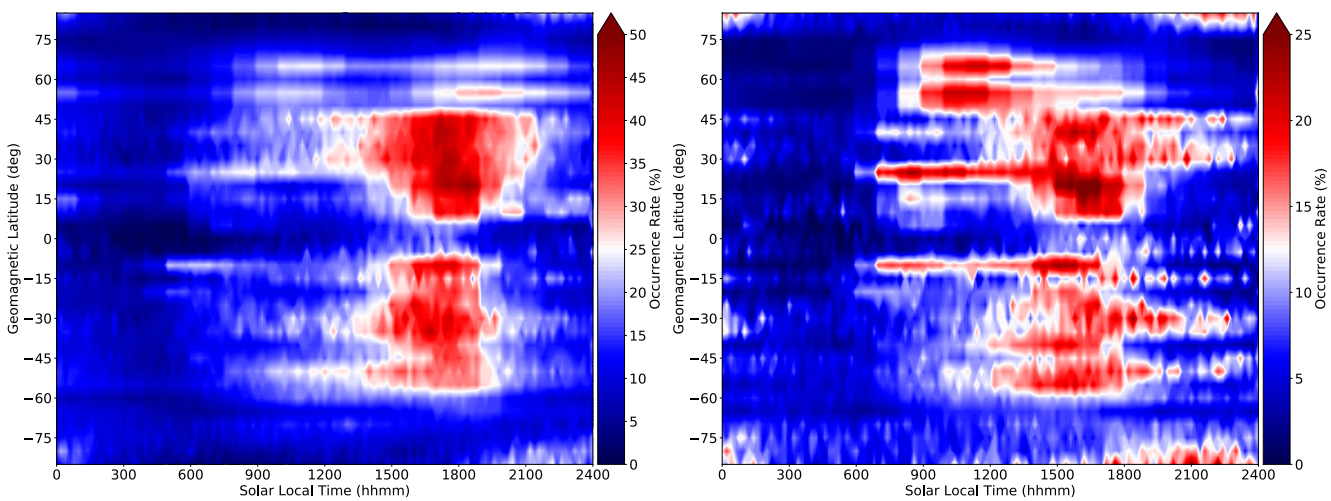

(a) All-E_s (b) Moderate-E_s

Figure 10. The annual occurrence rates as a function of solar local time and geomagnetic latitude for (a) All-E_s and (b) Moderate-E_s.

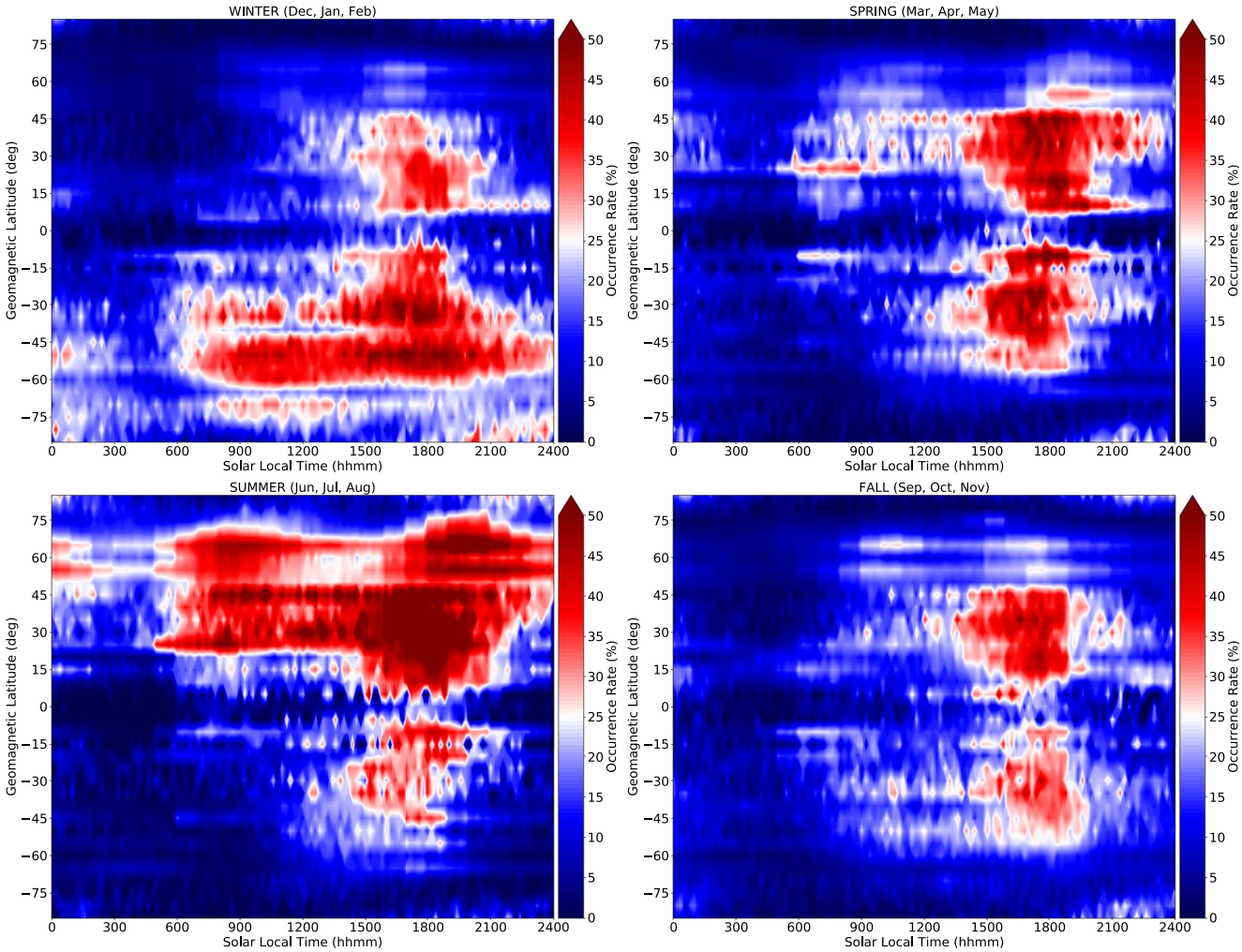

Figure 11. The all-E_s seasonal occurrence rates for solar local time and geomagnetic latitude.

in the respective hemispheres, the E_s primarily occurs in the late afternoon. Diurnal trends are similar for the moderate-E_s data set with a couple of noticeable differences. First, the high-latitudes show elevated rates relative to the mid-latitude peaks. Second, spring and fall rates are more pronounced in the morning relative to the all-E_s data set. This suggests that blanketing E_s formation in the morning is less frequent but stronger. The general diurnal trends are similar to the results by Wu et al. (2005), Chu et al. (2014), and Luo et al. (2021). The semidiurnal patterns observed in Wu et al. (2005) and Luo et al. (2021) for the local summer are also present in Figures 11 and 12. In the high-latitudes, there is a peak in the late evening and early morning time frame, which is in agreement with Whitehead (1970) and Luo et al. (2021). The observed trends can be explained by diurnal and semidiurnal wind shears, as simulated and described in detail in previous studies (e.g., Chu et al., 2014; Luo et al., 2021). In addition to the diurnal and semidiurnal tides, Haldoupis et al. (2004) showed that terdiurnal (8-hr period) and planetary waves (periods on the order of days) also influence sporadic-E.

4. Discussion

While the OR trends with respect to geomagnetic latitude closely follow the zonal wind shear theory, the longitudinal trends are not well understood. As displayed in Figures 4 and 5, large changes in OR occur over relatively small longitudinal distances for constant geomagnetic latitudes. This same general behavior with depleted and enhanced patches along constant geomagnetic latitudes is also displayed in previous GPS-RO (Arras & Wickert, 2018; Chu et al., 2014; Wu et al., 2005) and ionosonde (Merriman et al., 2021; Smith, 1957) derived climatologies. While the Northern Hemisphere for the all-E_s rates in Figure 5 shows less relative variation along

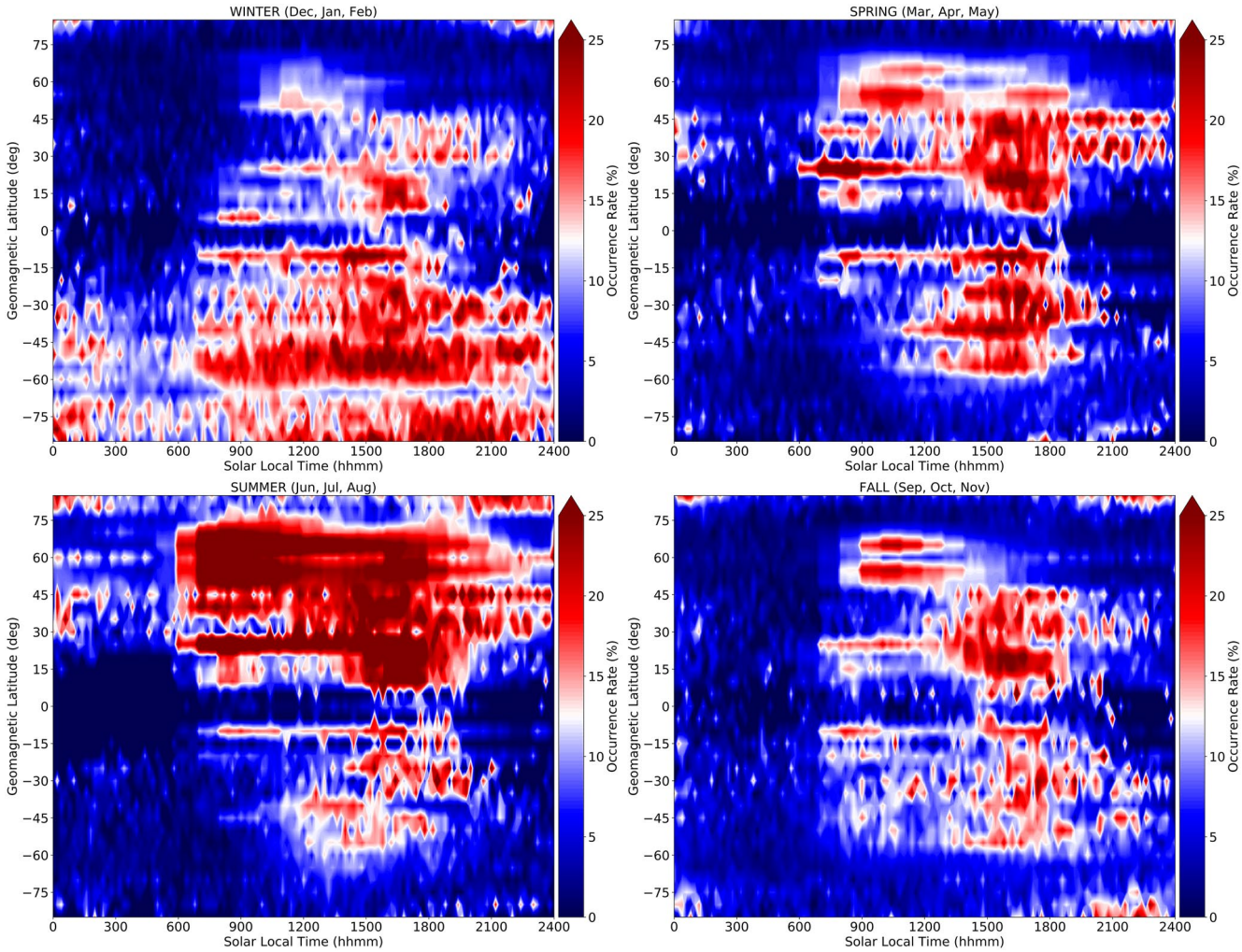

Figure 12. The moderate-E_s seasonal occurrence rates for solar local time and geomagnetic latitude.

longitude, the Southern Hemisphere shows substantial variation, likely due to the SAA. This variation is more extreme for the moderate-E_s ORs, which show complex longitudinal patterns within the mid-latitude envelope.

Much of the longitudinal variation can be described by the spatial dependence of diurnal and semidiurnal tidal wind shears (Chu et al., 2014; Luo et al., 2021; Shinagawa et al., 2017; Yu et al., 2019). Regional variations caused by atmospheric gravity waves (Sun, Hu, et al., 2021), local meteoric metal input/transport/chemistry (Feng et al., 2013; MacDougall et al., 2000; Yeh et al., 2014; Yu et al., 2021), and ionospheric electric fields (Huba et al., 2019; Nygren et al., 1984; Resende et al., 2016) also affect ORs. Additionally, Kelvin-Helmholtz instabilities inherent in sporadic-E formation (Bernhardt, 2002) can create billowy layers with small-scale structure (Hysell et al., 2012; Maeda & Heki, 2015; Sun, Zhao, et al., 2021). This small-scale structure can create patchy/cloudy layers with large changes in density over relatively short distances, which affects both ionosonde fbEs and GPS-RO measurements. However, the first-order trends follow the zonal wind shear theory fairly well and the regional contributions may be second-order contributions to sporadic-E formation rates.

Compared to previous GPS-RO climatological studies of E_s ORs (Arras & Wickert, 2018; Chu et al., 2014; Luo et al., 2021; Tsai et al., 2018; Wu et al., 2005; Yu et al., 2019), this study has some noticeable similarities and differences. The primary difference is the specification of sporadic-E intensities used in this analysis, which is not mentioned or unknown in previous GPS-RO derived climatologies. Concerning the input data used to develop the climatologies, we use data from 2006 to 2019 and incorporated 3.2 million Digisonde observations in addition to the GPS-RO data, which has not been included in previous GPS-RO derived E_s climatologies. The peak E_s ORs

for Arras and Wickert (2018) were in the 50%–60% range, in agreement with the all-E_s rates from this study. Luo et al. (2021) predicted peak ORs near 90% using an S_4 based technique with a threshold of 0.5, which is larger than our predicted peak rates using an S_4 threshold of 0.66 for all-E_s. Chu et al. (2014) provides the basis for the moderate-E_s technique in the study, so by no surprise, the ORs presented are similar to the moderate-E_s rates. However, the Chu et al. (2014) technique was slightly modified for this study by extending the allowed $\Delta L1/\Delta L2$ excess phase ratio to 1.2–1.9 from the original 1.5–1.8. Thus, the Chu et al. (2014) peak ORs are 5%–10% less than the moderate-E_s rates from this study on average.

Concerning spatial variability, the overall global trends we show here align well with the results from the previous studies showing peak E_s formation in the mid-latitudes with lower rates near the geomagnetic equator and SAA. The low ORs in the geomagnetic equator and SAA are clearly defined. Additionally, the decreased rates over North America is observed in all the climatological studies. Interestingly, we show significantly more high-latitude E_s activity than the previous climatologies for the moderate-E_s ORs. The global trends are in close agreement with the recent empirical model presented in Yu et al. (2022).

Seasonal variability is consistent throughout the various GPS-RO climatologies with a strong peak in mid-latitudes during local summer. In agreement with Chu et al. (2014), Yu et al. (2019), and Luo et al. (2021), the boreal spring ORs are slightly larger than the fall ORs and tend to form closer to the geomagnetic equator than during summer and winter. This is likely due to the general asymmetry observed between hemispheres caused by the weaker average horizontal magnetic field in the Southern Hemisphere due to the SAA, which induces an asymmetry in rates for both local summer (winter) and spring (fall). The lower thermospheric winter-to-summer transport described in (Yu et al., 2021) is clearly visible in the monthly ORs (Figures 8 and 9) as the peak OR bands move from local summer mid-latitudes through the equator during spring/fall to the opposite hemisphere.

When comparing ORs for the two intensity thresholds, trends align very well for all regions within ±80° inclination. In the high-latitudes, typically greater than 80° inclination, stronger but less frequent E_s is observed. Both RO techniques show nearly the same rates at these high-latitudes, indicating that high-latitude blanketing E_s is stronger but more rare. However, without an ionosonde present in this region for validation, there is a possibility that both RO techniques are measuring auroral activity instead of blanketing E_s. Auroral E-region enhancements are much thicker than sporadic-E, on the order of tens of kilometers (Basu et al., 1993) compared to kilometers for E_s (Zeng & Sokolovskiy, 2010). These thicker layers can induce large phase perturbations to the GPS-RO signal, but may result in weak amplitude scintillation because of the lens thickness with relatively small altitude gradients in electron density (Stambovsky et al., 2021; Wu, 2006). The strong dependence of the high-latitude region ORs on geomagnetic activity (to be discussed in detail in a subsequent paper) indicates that auroral-E is likely being detected instead of blanketing E_s. Additionally, the ionosonde derived foEs and fbEs rates provided by Merriman et al. (2021) include observations at Qaanaaq, Greenland with a magnetic inclination of ~85°, and the ORs show a decrease at this high-latitude station for both the all-E_s and fbEs ≥ 3 MHz thresholds. Without a direct comparison between GPS-RO and ionosonde measurements in this region, it is difficult to determine the trigger and additional research is required to examine the cause.

5. Conclusions

Observations from 46 Digisonde sites and COSMIC-I GPS-RO measurements from September 2006 to January 2019 were combined to provide a global E_s climatology for two intensity thresholds: fbEs with no low limit on intensity (all-E_s) and fbEs ≥ 3 MHz (moderate-E_s). Following the results of many previous sporadic-E climatologies, E_s ORs are found to be most prevalent between 10° and 60° geomagnetic latitude. Within the SAA, the large geomagnetic inclination angle and reduced magnetic field strength inhibits E_s formation in agreement with the wind shear theory. Likewise, along the geomagnetic equator, there is a distinct lack of E_s formation.

While the zonal wind shear theory can describe the general latitudinal behavior and some of the complex longitudinal trends, there are large variations in ORs observed over relatively small longitudinal distances indicating that other factors such as atmospheric gravity waves, local meteoric input, metallic ion transport, and ionospheric electric fields may affect observed ORs. High-latitude blanketing E_s is found to be stronger but less frequent with ORs nearly equal to the moderate-E_s mid-latitude maximums. However, without an ionosonde present in these regions for validation, more research is required to determine if auroral-E is being detected instead of blanketing E_s.

Seasonally, E_s ORs are elevated during the summer months for each hemisphere with peak ORs of ∼50% for all-E_s and 25% for moderate-E_s. The boreal spring and fall seasons are characterized by low E_s ORs worldwide. Elevated ORs are observed for most of the local summer mid-latitudes except within the SAA and over North America. The anomalous region over North America has rates 10%–15% lower than the rest of the Northern Hemisphere mid-latitude region likely due to an anomalous geographical dependence of vertical wind shear over North America (Shinagawa et al., 2017). Monthly, E_s ORs are highest in the Southern Hemisphere from November through February, and in the Northern Hemisphere from May through August. March, April, September, and October are the transition seasons when the large band of high E_s ORs would be over the equatorial region, but the geomagnetic equator inhibits the formation of E_s. The moderate-E_s ORs are about half of the all-E_s rates on average, except at high-latitudes.

Diurnally, blanketing E_s peaks in the late afternoon for most mid-latitudes. The all-E_s ORs show a maximum between 1600 and 1800 SL and the moderate-E_s set show a maximum from 1500 to 1700 SL. Additionally, the moderate-E_s show elevated late morning rates relative to the afternoon peaks indicating that blanketing E_s formation in the morning is less frequent but stronger. These stronger E_s layers also tend to last longer throughout the night, and there is evidence of significant high-latitude E_s from 1900 to 0200 SL. For the hemisphere in the summer season, E_s ORs are enhanced nearly the entire day with a gap in formation between 0200 and 0600 SL.

The solar cycle and geomagnetic activity dependence of global sporadic-E ORs will be explored in a subsequent paper. While this effort provides an updated sporadic-E climatology using a large input data set, there are a couple of key tasks that would be helpful for improving the estimates. First, this study does not take the background E-region into account, which shows a large diurnal variation and enhances daytime sporadic-E intensities (see Haldoupis (2019) for a detailed discussion). This background E-region fluctuation should be considered to focus solely on the sporadic-E perturbation. Additionally, there are instances in the seasonal and diurnal trends where the ionosonde and RO derived rates do not perfectly align. This same behavior was observed in the Carmona et al. (2022) comparison and indicates that fine-tuning RO techniques to match ionosonde observations will help improve global E_s climatologies. Finally, while a couple of E_s intensity thresholds were analyzed in this study, future efforts should include a wider range of intensities by focusing on intensity distributions over time to provide more detailed information on both formation and strength.

Data Availability Statement

The GPS radio occultation data used in the study is available at the COSMIC Data Analysis and Archive Center (CDAAC) via https://cdaac-www.cosmic.ucar.edu/ and the Digisonde data is available at the Digital Ionogram Database (DIDBase) via https://ulcar.uml.edu/DIDBase/.

Acknowledgments
We would like to thank the Digital Ionogram Database (https://ulcar.uml.edu/DIDBase/) and the COSMIC Data Analysis and Archive Center (https://cdaac-www.cosmic.ucar.edu/) for the use of their data. This research was funded by the Air Force Office of Scientific Research (AFOSR/RTB1). The views, opinions, and/or findings expressed are those of the author and should not be interpreted as representing the official views or policies of the Department of Defense or the U.S. Government.

References

Arras, C., & Wickert, J. (2018). Estimation of ionospheric sporadic E intensities from GPS radio occultation measurements. *Journal of Atmospheric and Solar-Terrestrial Physics*, *171*, 60–63. https://doi.org/10.1016/j.jastp.2017.08.006

Basu, S., Basu, S., Eastes, R., Huffman, R., Daniell, R., Chaturvedi, P., et al. (1993). Remote sensing of auroral E region plasma structures by radio, radar, and UV techniques at solar minimum. *Journal of Geophysical Research*, *98*(A2), 1589–1602. https://doi.org/10.1029/92ja01655

Bates, D., & Dalgarno, A. (1962). Electronic recombination. *Pure and Applied Physics*, *13*, 245–271. https://doi.org/10.1016/B9780120814503500114

Bernhardt, P. A. (2002). The modulation of sporadic-E layers by kelvin–Helmholtz billows in the neutral atmosphere. *Journal of Atmospheric and Solar-Terrestrial Physics*, *64*(12–14), 1487–1504. https://doi.org/10.1016/s1364-6826(02)00086-x

Bossy, L. (1994). Accuracy comparison of ionogram inversion methods. *Advances in Space Research*, *14*(12), 39–42. https://doi.org/10.1016/0273-1177(94)90235-6

Buchert, S., Zangerl, F., Sust, M., André, M., Eriksson, A., Wahlund, J.-E., & Opgenoorth, H. (2015). Swarm observations of equatorial electron densities and topside GPS track losses. *Geophysical Research Letters*, *42*(7), 2088–2092. https://doi.org/10.1002/2015gl063121

Carmona, R. A., Nava, O. A., Dao, E. V., & Emmons, D. J. (2022). A comparison of sporadic-E occurrence rates using GPS radio occultation and ionosonde measurements. *Remote Sensing*, *14*(3), 581. https://doi.org/10.3390/rs14030581

Cathey, E. H. (1969). Some midlatitude sporadic-E results from the explorer 20 satellite. *Journal of Geophysical Research*, *74*(9), 2240–2247. https://doi.org/10.1029/ja074i009p02240

Ceplecha, Z., Borovička, J., Elford, W. G., ReVelle, D. O., Hawkes, R. L., Porubčan, V., & Šimek, M. (1998). Meteor phenomena and bodies. *Space Science Reviews*, *84*(3), 327–471. https://doi.org/10.1023/a:1005069928850

Chu, Y. H., Wang, C. Y., Wu, K. H., Chen, K. T., Tzeng, K. J., Su, C. L., et al. (2014). Morphology of sporadic E layer retrieved from cosmic GPS radio occultation measurements: Wind shear theory examination. *Journal of Geophysical Research: Space Physics*, *119*(3), 2117–2136. https://doi.org/10.1002/2013JA019437

Coleman, C. J. (1998). A ray tracing formulation and its application to some problems in over-the-horizon radar. *Radio Science*, *33*(4), 1187–1197. https://doi.org/10.1029/98rs01523

Conceição-Santos, F., Muella, M. T., Resende, L. C., Fagundes, P. R., Andrioli, V. F., Batista, P. P., et al. (2019). Occurrence and modeling examination of sporadic-E layers in the region of the South America (Atlantic) magnetic anomaly. *Journal of Geophysical Research: Space Physics*, *124*(11), 9676–9694. https://doi.org/10.1029/2018ja026397

Davies, K., & Hartmann, G. K. (1997). Studying the ionosphere with the global positioning system. *Radio Science*, *32*(4), 1695–1703. https://doi.org/10.1029/97rs00451

Feng, W., Marsh, D. R., Chipperfield, M. P., Janches, D., Höffner, J., Yi, F., & Plane, J. M. (2013). A global atmospheric model of meteoric iron. *Journal of Geophysical Research: Atmospheres*, *118*(16), 9456–9474. https://doi.org/10.1002/jgrd.50708

Fong, C.-J., Yang, S.-K., Chu, C.-H., Huang, C.-Y., Yeh, J.-J., Lin, C.-T., et al. (2008). Formosat-3/cosmic constellation spacecraft system performance: After one year in orbit. *IEEE Transactions on Geoscience and Remote Sensing*, *46*(11), 3380–3394. https://doi.org/10.1109/tgrs.2008.2005203

Galkin, I. A., & Reinisch, B. W. (2008). The new artist 5 for all digisondes. *Ionosonde Network Advisory Group Bulletin*, *69*(8), 1–8.

Gooch, J. Y., Colman, J. J., Nava, O. A., & Emmons, D. J. (2020). Global ionosonde and GPS radio occultation sporadic-E intensity and height comparison. *Journal of Atmospheric and Solar-Terrestrial Physics*, *199*, 105200. https://doi.org/10.1016/j.jastp.2020.105200

Haldoupis, C. (2011). A tutorial review on sporadic E layers. *Aeronomy of the Earth's Atmosphere and Ionosphere*, 381–394. https://doi.org/10.1007/978-94-007-0326-1_29

Haldoupis, C. (2019). An improved ionosonde-based parameter to assess sporadic E layer intensities: A simple idea and an algorithm. *Journal of Geophysical Research: Space Physics*, *124*(3), 2127–2134. https://doi.org/10.1029/2018ja026441

Haldoupis, C., Pancheva, D., & Mitchell, N. (2004). A study of tidal and planetary wave periodicities present in midlatitude sporadic E layers. *Journal of Geophysical Research*, *109*(A2), A02302. https://doi.org/10.1029/2003ja010253

Haldoupis, C., Pancheva, D., Singer, W., Meek, C., & MacDougall, J. (2007). An explanation for the seasonal dependence of midlatitude sporadic E layers. *Journal of Geophysical Research*, *112*(A6), A06315. https://doi.org/10.1029/2007JA012322

Headrick, J. M., Anderson, S. J., & Skolnik, M. (2008). *HF over-the-horizon radar*. Radar handbook, 20

Huba, J., Krall, J., & Drob, D. (2019). Global ionospheric metal ion transport with SAMI3. *Geophysical Research Letters*, *46*(14), 7937–7944. https://doi.org/10.1029/2019gl083583

Hysell, D., Nossa, E., Larsen, M., Munro, J., Smith, S., Sulzer, M., & González, S. (2012). Dynamic instability in the lower thermosphere inferred from irregular sporadic E layers. *Journal of Geophysical Research*, *117*(A8), 13. https://doi.org/10.1029/2012ja017910

Hysell, D., Nossa, E., Larsen, M., Munro, J., Sulzer, M., & González, S. (2009). Sporadic E layer observations over arecibo using coherent and incoherent scatter radar: Assessing dynamic stability in the lower thermosphere. *Journal of Geophysical Research*, *114*(A12), A12303. https://doi.org/10.1029/2009ja014403

Janches, D., Heinselman, C. J., Chau, J. L., Chandran, A., & Woodman, R. (2006). Modeling the global micrometeor input function in the upper atmosphere observed by high power and large aperture radars. *Journal of Geophysical Research*, *111*(A7), A07317. https://doi.org/10.1029/2006ja011628

Kamide, Y., & Akasofu, S.-I. (1983). Notes on the auroral electrojet indices. *Reviews of Geophysics*, *21*(7), 1647–1656. https://doi.org/10.1029/rg021i007p01647

Kintner, P. M., Ledvina, B. M., & Paula, E. R. D. (2007). *GPS and ionospheric scintillations* (Vol. 5). Space weather.

Luo, J., Liu, H., & Xu, X. (2021). Sporadic E morphology based on cosmic radio occultation data and its relationship with wind shear theory. *Earth Planets and Space*, *73*(1), 1–17. https://doi.org/10.1186/s40623-021-01550-w

MacDougall, J. W., Plane, J. M. C., & Jayachandran, P. T. (2000). Polar cap sporadic-E: Part 2, modeling. *Journal of Atmospheric and Solar-Terrestrial Physics*, *62*(13), 1169–1176. https://doi.org/10.1016/s1364-6826(00)00092-4

Maeda, J., & Heki, K. (2015). Morphology and dynamics of daytime mid-latitude sporadic-E patches revealed by GPS total electron content observations in Japan aeronomy. *Earth Planets and Space*, *67*(1), 1–9. https://doi.org/10.1186/s40623-015-0257-4

Mathews, J. D. (1998). Sporadic E: Current views and recent progress. *Journal of Atmospheric and Solar-Terrestrial Physics*, *60*(4), 413–435. https://doi.org/10.1016/s1364-6826(97)00043-6

Matsushita, S., & Reddy, C. A. (1967). A study of blanketing sporadic E at middle latitudes. *Journal of Geophysical Research*, *72*(11), 2903–2916. https://doi.org/10.1029/jz072i011p02903

Maus, S., Macmillan, S., McLean, S., Hamilton, B., Thomson, A., Nair, M., & Rollins, C. (2010). The US/UK world magnetic model for 2010–2015.

Merriman, D. K., Nava, O. A., Dao, E. V., & Emmons, D. J. (2021). Comparison of seasonal foes and FBES occurrence rates derived from global digisonde measurements. *Atmosphere*, *12*, 1558. https://doi.org/10.3390/atmos12121558

Neubeck, K. E. (1996). Using the combined resources of amateur radio observations and ionosonde data in the study of temperate zone sporadic-E. *Journal of Atmospheric and Terrestrial Physics*, *58*(12), 1355–1365. https://doi.org/10.1016/0021-9169(95)00170-0

Niu, J., Weng, L. B., Meng, X., & Fang, H. X. (2019). Morphology of ionospheric sporadic E layer intensity based on cosmic occultation data in the midlatitude and low-latitude regions. *Journal of Geophysical Research: Space Physics*, *124*(6), 4796–4808. https://doi.org/10.1029/2019ja026828

Nygren, T., Jalonen, L., Oksman, J., & Turunen, T. (1984). The role of electric field and neutral wind direction in the formation of sporadic E-layers. *Journal of Atmospheric and Terrestrial Physics*, *46*(4), 373–381. https://doi.org/10.1016/0021-9169(84)90122-3

Piggott, W., & Rawer, K. (1978). URSI handbook of ionogram interpretation and reduction. 1961.

Reddy, C., & Mukunda Rao, M. (1968). On the physical significance of the ES parameters FBES, FES, and FOES. *Journal of Geophysical Research*, *73*(1), 215–224. https://doi.org/10.1029/ja073i001p00215

Reinisch, B. W., & Galkin, I. A. (2011). Global ionospheric radio observatory (GIRO). *Earth Planets and Space*, *63*(4), 377–381. https://doi.org/10.5047/eps.2011.03.001

Resende, L. C. A., Batista, I. S., Denardini, C. M., Carrasco, A. J., de Fátima Andrioli, V., Moro, J., et al. (2016). Competition between winds and electric fields in the formation of blanketing sporadic E layers at equatorial regions. *Earth Planets and Space*, *68*(1), 1–14. https://doi.org/10.1186/s40623-016-0577-z

Rice, D. D., Sojka, J. J., Eccles, J. V., Raitt, J. W., Brady, J. J., & Hunsucker, R. D. (2011). *First results of mapping sporadic E with a passive observing network* (Vol. 9). Space Weather.

Rishbeth, H., & Garriott, O. K. (1969). *Introduction to ionospheric physics*. Academic Press.

Ritchie, S. E., & Honary, F. (2009). Observations on the variability and screening effect of sporadic-E. *Journal of Atmospheric and Solar-Terrestrial Physics*, *71*(12), 1353–1364. https://doi.org/10.1016/j.jastp.2009.05.008

Rocken, C., Ying-Hwa, K., Schreiner, W. S., Hunt, D., Sokolovskiy, S., & McCormick, C. (2000). Cosmic system description. *Terrestrial, Atmospheric and Oceanic Sciences*, *11*(1), 21–52. https://doi.org/10.3319/tao.2000.11.1.21(cosmic)

Schreiner, B., Kuo, B., Rocken, C., Sokolovskiy, S., Hunt, D., Ho, B., et al. (2014). Cosmic data analysis and archive center (CDAAC) current status and future plans. In *Eighth FormoSat-3/COSMIC data users' workshop*. National Science Foundation, National Space Organization and Taiwan, National Science Council Taiwan.

Schunk, R., & Nagy, A. (2009). *Ionospheres: Physics plasma physics, and chemistry* (2nd ed.). Cambridge University Press. https://doi.org/10.1017/cbo9780511635342

Shinagawa, H., Miyoshi, Y., Jin, H., & Fujiwara, H. (2017). Global distribution of neutral wind shear associated with sporadic E layers derived from GAIA. *Journal of Geophysical Research: Space Physics*, *122*(4), 4450–4465. https://doi.org/10.1002/2016ja023778

Singer, W., Zahn, U. V., & Weiß, J. (2004). Diurnal and annual variations of meteor rates at the Arctic circle. *Atmospheric Chemistry and Physics*, *4*(5), 1355–1363. https://doi.org/10.5194/acp-4-1355-2004

Smith, E. K. (1957). *Worldwide occurrence of sporadic E* (Vol. 582). US Department of Commerce, National Bureau of Standards

Stambovsky, D. W., Colman, J. J., Nava, O. A., & Emmons, D. J. (2021). Simulation of GPS radio occultation signals through sporadic-E using the multiple phase screen method. *Journal of Atmospheric and Solar-Terrestrial Physics*, *214*, 105538. https://doi.org/10.1016/j.jastp.2021.105538

Sun, W., Hu, L., Yang, Y., Zhao, X., Yang, S., Xie, H., et al. (2021). Occurrences of regional strong ES irregularities and corresponding scintillations characterized using a high-temporal-resolution GNSS network. *Journal of Geophysical Research: Space Physics*, *126*(11), e2021JA029460. https://doi.org/10.1029/2021ja029460

Sun, W., Zhao, X., Hu, L., Yang, S., Xie, H., Chang, S., et al. (2021). Morphological characteristics of thousand-kilometer-scale ES structures over China. *Journal of Geophysical Research: Space Physics*, *126*(2), e2020JA028712. https://doi.org/10.1029/2020ja028712

Syndergaard, S. (2006). *Cosmic S4 data*. UCAR/CDAAC.

Tsai, L.-C., Su, S.-Y., Liu, C.-H., Schuh, H., Wickert, J., & Alizadeh, M. M. (2018). Global morphology of ionospheric sporadic E layer from the formosat-3/cosmic GPS radio occultation experiment. *GPS Solutions*, *22*(4), 1–12. https://doi.org/10.1007/s10291-018-0782-2

Whitehead, J. D. (1970). Production and prediction of sporadic E. *Reviews of Geophysics*, *8*(1), 65–144. https://doi.org/10.1029/rg008i001p00065

Whitehead, J. D. (1972). The structure of sporadic E from a radio experiment. *Radio Science*, *7*(3), 355–358. https://doi.org/10.1029/rs007i003p00355

Whitehead, J. D. (1989). Recent work on mid-latitude and equatorial sporadic-E. *Journal of Atmospheric and Terrestrial Physics*, *51*(5), 401–424. https://doi.org/10.1016/0021-9169(89)90122-0

Wu, D. L. (2006). Small-scale fluctuations and scintillations in high-resolution GPS/champ SNR and phase data. *Journal of Atmospheric and Solar-Terrestrial Physics*, *68*(9), 999–1017. https://doi.org/10.1016/j.jastp.2006.01.006

Wu, D. L., Ao, C. O., Hajj, G. A., Juarez, M. D. L. T., & Mannucci, A. J. (2005). Sporadic E morphology from GPS-champ radio occultation. *Journal of Geophysical Research*, *110*(A1), A01306. https://doi.org/10.1029/2004JA010701

Yamazaki, Y., Arras, C., Andoh, S., Miyoshi, Y., Shinagawa, H., Harding, B., et al. (2022). Examining the wind shear theory of sporadic E with icon/mighti winds and cosmic-2 radio occultation data. *Geophysical Research Letters*, *49*(1), e2021GL096202. https://doi.org/10.1029/2021gl096202

Yang, K.-F., Chu, Y.-H., Su, C.-L., Ko, H.-T., & Wang, C.-Y. (2009). An examination of formosat-3/cosmic ionospheric electron density profile: Data quality criteria and comparisons with the iri model. *Terrestrial, Atmospheric and Oceanic Sciences*, *20*(1), 193. https://doi.org/10.3319/tao.2007.10.05.01(f3c)

Yeh, W.-H., Liu, J.-Y., Huang, C.-Y., & Chen, S.-P. (2014). Explanation of the sporadic-E layer formation by comparing formosat-3/cosmic data with meteor and wind shear information. *Journal of Geophysical Research: Atmospheres*, *119*(8), 4568–4579. https://doi.org/10.1002/2013jd020798

Younger, P., Astin, I., Sandford, D. J., & Mitchell, N. J. (2009). The sporadic radiant and distribution of meteors in the atmosphere as observed by VHF radar at Arctic, Antarctic and equatorial latitudes. *Annales Geophysicae*, *27*(7), 2831–2841. https://doi.org/10.5194/angeo-27-2831-2009

Yu, B., Scott, C. J., Xue, X., Yue, X., & Dou, X. (2020). Derivation of global ionospheric sporadic E critical frequency (foes) data from the amplitude variations in GPS/GNSS radio occultations. *Royal Society Open Science*, *7*, 200320. https://doi.org/10.1098/rsos.200320

Yu, B., Xue, X., Scott, C. J., Wu, J., Yue, X., Feng, W., et al. (2021). Interhemispheric transport of metallic ions within ionospheric sporadic E layers by the lower thermospheric meridional circulation. *Atmospheric Chemistry and Physics*, *21*(5), 4219–4230. https://doi.org/10.5194/acp-21-4219-2021

Yu, B., Xue, X., Scott, C. J., Yue, X., & Dou, X. (2022). An empirical model of the ionospheric sporadic E layer based on GNSS radio occultation data. *Space Weather*, *20*(8), e2022SW003113. https://doi.org/10.1029/2022sw003113

Yu, B., Xue, X., Yue, X., Yang, C., Yu, C., Dou, X., et al. (2019). The global climatology of the intensity of the ionospheric sporadic E layer. *Atmospheric Chemistry and Physics*, *19*(6), 4139–4151. https://doi.org/10.5194/acp-19-4139-2019

Yue, X., Schreiner, W. S., Kuo, Y.-H., Wu, Q., Deng, Y., & Wang, W. (2013). GNSS radio occultation (RO) derived electron density quality in high latitude and polar region: NCAR-TIEGCM simulation and real data evaluation. *Journal of Atmospheric and Solar-Terrestrial Physics*, *98*, 39–49. https://doi.org/10.1016/j.jastp.2013.03.009

Zeng, Z., & Sokolovskiy, S. (2010). Effect of sporadic E clouds on GPS radio occultation signals. *Geophysical Research Letters*, *37*(18). https://doi.org/10.1029/2010GL044561